*Journal of Zhejiang University-SCIENCE A (Applied Physics & Engineering)* *2024 25(11):938-952*
www.jzus.zju.edu.cn; www.springer.com/journal/11582
E-mail: jzus_a@zju.edu.cn

**Research Article**
https://doi.org/10.1631/jzus.A2300288



# Distribution law analysis and calculating method for windage power in a geotechnical centrifuge

Chuanxiang ZHENG[1], Yuchen DAI[1]✉, Jiao LIN[1], Jianqun JIANG[1], Jinjie LU[1], Zhenyu WANG[1], Jiaming YAN[2]

[1]*College of Energy Engineering, Zhejiang University, Hangzhou 310027, China*
[2]*Huadong Engineering Co. Ltd., Hangzhou 300450, China*

**Abstract:** Temperature rise caused by windage power is a major limitation to the large-scale process of geotechnical centrifuges. However, there is no consensus on how to identify the key parts (parts with high windage power consumption) and parameters (the velocity coefficient $\alpha$ and windage coefficient $C_f$), and the influence of idle power is often neglected in methods for calculating windage power. To address these issues, a Centrifugal Hypergravity and Interdisciplinary Experiment Facility (CHIEF) scaled model device was constructed, and the windage power was measured. Then, a computational fluid dynamics (CFD) model of the device was established and validated by experimental results. Simulation results were analyzed to quantify the proportion of the windage power in different parts of the device and summarize the variation law of key parameters. Finally, a novel windage power calculation equation was developed based on the elimination of the influence of the idle power. Results show that the role of the rotating arm cannot be ignored in the selection of key parts. The velocity coefficient and windage coefficient are a function of the device geometry and size, and are independent of the angular velocity. The windage power is proportional to the cube of the angular velocity after eliminating the effect of idle power.

**Key words:** Geotechnical centrifuge; Windage power; Key parts and parameters; Centrifugal Hypergravity and Interdisciplinary Experiment Facility (CHIEF); Idle power

## 1 Introduction

A geotechnical centrifuge is an important piece of equipment used in geotechnical engineering to study geological disasters, underground engineering, railway construction, and other issues (Lee and Schofield, 1988; Watson and Randolph, 1998; Leung et al., 2001; White et al., 2003; Lee et al., 2006; Garnier et al., 2007; Najser et al., 2009; Take and Bolton, 2011; Deng et al., 2012; Iglesia et al., 2014; Garzón et al., 2015; Costa et al., 2016; Liang et al., 2017; Balakrishnan and Viswanadham, 2019; Zhang et al., 2021; Chanda et al., 2023; Gao et al., 2023). A typical geotechnical centrifuge consists of a rotating arm, experiment basket, pedestal, and balance weight basket (Fig. 1). When the equipment is operating, the rotating arm rotates at a high speed, making the baskets on both sides swing to a position in line with the rotating arm under the centrifugal force, and the sample in the basket is in a state of hypergravity under the effect of the centrifuge acceleration. Higher centrifugal acceleration, higher effective capacity, and a larger radius of rotation of the rotating arm can expand the spatial scale and temporal scale of the study object. Thus, the geotechnical centrifuge is evolving toward large-scale operations (Zeng and Lim, 2002; Song et al., 2019; Ng et al., 2020; Woodward et al., 2022; Dai et al., 2023). However, the windage power will sharply increase with the growth in the size of the geotechnical centrifuge since it accounts for more than 80% of the total driving power. The resulting temperature rise will be more significant and become a crucial constraint in large-scale processes (Sun, 1991; Zhang et al., 2019; Lin et al., 2020; Zheng et al., 2020; Shao et al., 2022; Yan et al., 2022; Zhu and Dai, 2023). Recently the world's largest geotechnical centrifuge, the Centrifugal Hypergravity and Interdisciplinary Experiment Facility (CHIEF), was constructed by Zhejiang University, China. This

✉ Yuchen DAI, dustree@zju.edu.cn
Chuanxiang ZHENG, https://orcid.org/0000-0002-8904-0943
Yuchen DAI, https://orcid.org/0000-0002-9636-7493

Received June 27, 2023; Revision accepted Feb. 2, 2024;
Crosschecked Oct. 14, 2024; Online first Nov. 21, 2024

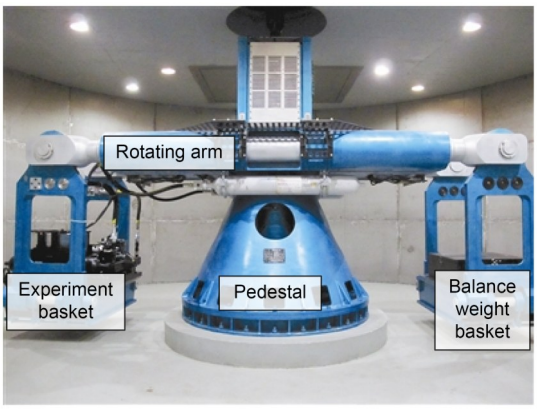


**Fig. 1 Structure of a typical geotechnical centrifuge**

facility will have an effective capacity of 2200*g* (in metric ton) and a maximum acceleration of 1500*g* (*g* is the acceleration of gravity). Controlling the temperature of the machine room at (40±5) °C is one of the key technologies that need to be solved urgently during the construction of the device. The key to temperature control design is to accurately calculate the windage power (Jia, 2013; Lin et al., 2020; Guo et al., 2021).

When calculating the windage power of a geotechnical centrifuge, it is necessary first to figure out which parts are subject to greater windage (usually including the rotating arm and the basket). The geometric shape of a part, such as the windward wall, the leeward wall or the side wall of the basket, can affect the windage power. These are regarded as key parts and regions. In addition, the density of the air in the machine room, the air rotation speed in different regions, and the windage coefficient $C_i$ of the parts have an influence on the windage power. The air rotation speed is usually described by the velocity coefficient $\alpha$, which represents the air rotating at $\alpha$ times the rotor speed. Since the values of these parameters have a great impact on the results of windage power calculation, it is essential to explore these key parameters in detail.

The difference between the various calculation methods lies mainly in the selection of the key parts (regions) $i$ and determination of the key parameters ($\alpha$, $C_i$) (Kutter et al., 1991; Du et al., 1992; Yin et al., 2010a, 2010b; Hao et al., 2018; Yin et al., 2018, 2020; Chen et al., 2020). In terms of part selection, according to the method of Acutronic (Hao et al., 2018), the windage power consumed on the basket accounts for most of the total windage power, so only the basket was considered. The АзНИИСМиС Institute (Jia, 2013) considered the influence of the rotating arm and the basket simultaneously and manufactured a scaled model integrating them for experimental exploration. The China Academy of Engineering Physics (CAEP) has made a more detailed distinction, which divides the rotating arm walls into the windward wall, leeward wall, and downwind wall (Yin et al., 2010a, 2010b). However, these methods are more of a qualitative nature and a quantitative study is necessary to identify the key parts (regions) that affect the windage power. In terms of key parameter determination, there are two sorts of approaches. One is to regard $\alpha$ and $C_i$ as inherent parameters of the device and as constants, as in the Acutronic and UC Davis methods. The other is to consider $\alpha$ and $C_i$ to be related to the angular velocity $\omega$ of the rotating arm. For example, the CAEP method posits that $C_i$ is related to the flow state of the air near the wall, and derives the $C_i$ equation related to $\omega$. The АзНИИСМиС Institute method regards $\alpha$ and $C_i$ as a combined coefficient $A_i$. $A_i$ is considered a function of $\omega$ by the analysis of the total power at different speeds measured in the test. However, the effect of the rotor radius on $\alpha$ and $C_i$ is neglected in these methods. In addition to the windage, geotechnical centrifuge power is also consumed by the losses from the motor and the friction of the mechanical transmission system, collectively known as idle power. It is hard to disassemble the rotating arm system of a geotechnical centrifuge once it has been installed, which makes it difficult to measure the device's idle power. Therefore, the idle power of the equipment is usually ignored (Yin et al., 2010a; Wang et al., 2014; Guo et al., 2020a, 2020b, 2021). Since the effect caused by the idle power was not excluded in previous studies, the formula described may not be applicable to the windage power. It is for these reasons that the current calculation method is not universal. It may produce a large error when the key parameter law obtained from a specific device is applied to other devices.

To acquire a universal windage power distribution law and calculation method, a scaled model device that takes CHIEF high-speed equipment as the prototype was constructed in this research. Accurate windage power was measured and used to calibrate the numerical model after the impact of idle power was removed and the transmission error was assessed. Following this, a novel windage power calculation method was presented, and key part selection and the variation

rules of key parameters were explored. Ultimately, the impact of idle power on the form of the windage power function was examined, and the adaptability of the suggested approach was confirmed through the use of experimental data from three actual geotechnical centrifuges.

## 2 Scaled model experiment

The inaccurate calculation of the windage power is due largely to the failure to exclude the influence of idle power. Therefore, to eliminate the influence of the idle power, in this study an indirect measurement scheme was proposed, and an experimental study based on the CHIEF high-speed scaled model device was conducted. In addition, the transmission error introduced by the indirect measurement method was evaluated.

### 2.1 Measurement solutions of windage power

The basket and rotating arm of the CHIEF high-speed machine are combined into one part known as the rotor, since their section heights are the same. A schematic diagram of the scaled model device is shown in Fig. 2. In Fig. 2a, an isolation room is formed by the machine room walls and the cover, in which the rotor and shaft are driven by the motor to rotate. The actual experimental device is shown in Fig. 2b. The diameter and height of the machine room are each 600 mm. The actual rotor is shown in Fig. 2c, with an outer diameter of 470 mm and a height of 34 mm. The motor is linked to the measurement system (Fig. 2d). The protective enclosure is used to ensure the tester's safety.

When the device is running steadily, the input voltage ($U$), current ($I$), and motor speed ($n$) of the device can be measured by the measurement system. The total power can be calculated by the equation $P=UI$. The following test method was developed with two working conditions, namely, the idle power working condition (marked by subscript h) and the total power working condition to precisely quantify the windage power consumed on the rotor (indicated by subscript t). In addition, subscripts w and $j$ denote the windage power and different speeds, respectively. The two test conditions are described as follows:

**Working condition h:** Only the shaft was mounted on the device (no rotor). The voltage $U_{hj}$ and current $I_{hj}$ of the device were measured under steady operation at different speeds $n_j$.

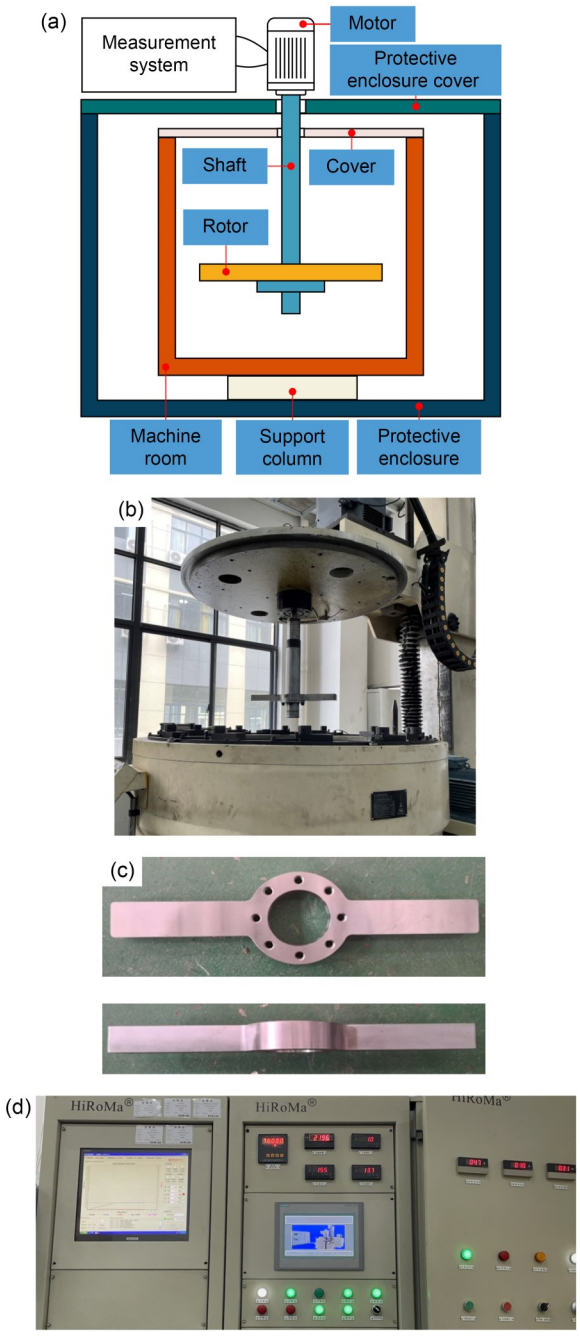


**Fig. 2 Schematic diagram of the scaled model device: (a) schematic diagram; (b) actual experimental device; (c) rotor; (d) measurement system**

**Working condition t:** Both the shaft and rotor were mounted on the device. The voltage $U_{tj}$ and current $I_{tj}$ of the device were measured under steady operation at different speeds $n_j$.

It is possible to calculate the idle power by $P_{hj}=U_{hj}I_{hj}$ at various speeds using the measurement results of the working condition h. Similarly, the total power

can be calculated by $P_{tj}=U_{tj}I_{tj}$, according to the working condition t. Since $P_{tj}$ includes the idle power and the windage power consumed on the rotor, the windage power can be obtained by subtracting the idle power from $P_{tj}$, i.e.,

$$P_{wj}=P_{tj}-P_{hj}=U_{tj}I_{tj}-U_{hj}I_{hj}. \tag{1}$$

Therefore, the windage moment $T_{wj}$ can be calculated by Eq. (2), where $\omega_j=2\pi n_j$, $T_{tj}$ is the total driving moment of the motor, and $T_{hj}$ is the moment of the motor in the idle state.

$$T_{wj}=T_{tj}-T_{hj}=\frac{U_{tj}I_{tj}}{\omega_j}-\frac{U_{hj}I_{hj}}{\omega_j}. \tag{2}$$

## 2.2 Error transfer

In the above test scheme, $U_{lj}$ (l=h, t), $I_{lj}$, and $n_j$ (equivalent to $\omega_j$) are directly measured physical quantities. $P_{lj}$, $P_{wj}$, and $T_{wj}$ are indirectly measured physical quantities. So, the error of directly measured quantities will be transferred to the indirectly measured quantities by the functional relationship between them. The error transfer process can be evaluated using the method of Dong (2013).

Assume that the functional relationship between the indirect measured quantity $y$ and the $N$ direct measured quantities $x_1$, $x_2$, ⋯, $x_N$ is as follows:

$$y=f(x_1, x_2, \cdots, x_N). \tag{3}$$

The $N$ direct measured quantities are measured $m$ times with equal accuracy in the test, and the measured values are:

$$\begin{aligned}
&x_1\colon x_{\{11\}}, x_{\{12\}}, \cdots, x_{\{1m\}},\\
&x_2\colon x_{\{21\}}, x_{\{22\}}, \cdots, x_{\{2m\}},\\
&\quad\vdots\qquad\qquad\vdots\\
&x_N\colon x_{\{N1\}}, x_{\{N2\}}, \cdots, x_{\{Nm\}}.
\end{aligned}$$

If the standard deviations for each measured value are $s_1$, $s_2$, ⋯, $s_N$, then the standard deviation after considering the error transfer is:

$$s=\sqrt{\sum_{i=1}^{N}(c_i s_i)^2+2\sum_{1\le i\le j}^{N} r_{ij}c_i c_j s_i s_j}, \tag{4}$$

where $c_i=\partial f/\partial x_i$, which is the error transfer coefficient of $x_i$; $r_{ij}=k_{ij}/[s_i\cdot s_j]$, which is the correlation coefficient between $x_i$ and $x_j$. $k_{ij}=\frac{1}{N}\sum_{m=1}^{N}\delta x_{im}\cdot\delta x_{jm}$, which is the covariance. $\delta x_{im}=x_{im}-\bar{x}_i$, where $\bar{x}_i$ is the average of $x_i$.

The $t$-distribution was used in our work to determine the limit error of each measurement quantity for the small sample test data, where the significance level was taken as $\alpha$=0.01 (i.e., 99% confidence). The confidence coefficient $t_\alpha$ can be obtained by looking up in a table, then the limit error of the indirectly measured quantity $y$ is:

$$\delta_{\lim y}=\pm t_\alpha s_{\bar{y}}, \tag{5}$$

where $\bar{y}$ is the average of the indirectly measured quantity and $s_{\bar{y}}$ is the standard deviation after considering error transfer. Then, the error of $y$ can be evaluated as:

$$e_y=\frac{\delta_{\lim y}}{\bar{y}}\times 100\%. \tag{6}$$

The error evaluation results of $P_w$ and $T_w$ are shown in Table 1, where $e_\omega$, $e_{Pw}$ and $e_{Tw}$ respectively represent the limit deviations of $\omega$, $P_w$, and $T_w$.

**Table 1 Error evaluation of $P_w$ and $T_w$**

| $\omega$ (rad/s) | $e_\omega$ (%) | $P_w$ (W) | $e_{Pw}$ (%) | $T_w$ (N·m) | $e_{Tw}$ (%) |
|---|---|---|---|---|---|
| 105.29 | 1.81 | 36.50 | 83.08 | 0.35 | 83.75 |
| 209.03 | 0.26 | 204.06 | 22.30 | 0.97 | 22.43 |
| 313.98 | 0.13 | 727.42 | 8.57 | 2.32 | 8.59 |
| 418.68 | 0.09 | 1750.12 | 2.91 | 4.18 | 2.92 |
| 523.56 | 0.05 | 3370.72 | 3.12 | 6.44 | 3.12 |
| 671.60 | 0.12 | 6825.11 | 1.46 | 10.16 | 1.47 |
| 733.04 | 0.07 | 8692.58 | 1.87 | 11.86 | 1.87 |
| 906.75 | 0.51 | 16345.88 | 1.40 | 18.11 | 1.40 |

Table 1 shows that the indirect measurement method will result in significant errors at low speed, but when $\omega$ is higher than 418.68 rad/s, the indirect measurement errors of $P_w$ and $T_w$ are lower than 5% (i.e., the error value allowed in general engineering). Therefore, it is important to assess the measurement method errors when using such indirect measurement techniques. In this study, the simulation model was verified using the measurement data when $\omega$ was larger than 418.68 rad/s.

## 3 Numerical model and validation

### 3.1 Establishment of calculation domain

The commercial computational fluid dynamics (CFD) solver ANSYS Fluent was used in this study to solve the three-dimensional, steady, and Reynolds-averaged Navier–Stokes (RANS) equations.

The calculation domain was taken to be the interior of the machine room which is regarded as a closed structure, ignoring the gap between the shaft and the cover and the steps at shaft–rotor bolted connections. Since the rotating system in the scaled model has an axisymmetric periodic domain, the rotating periodic conditions were imposed to save computation time. So, the calculation model was taken as half of the actual model (Fig. 3). "Period 1" and "Period 2" in Fig. 3c are a pair of periodic boundary interfaces. The machine room and rotor wall surfaces are labeled as indicated in Figs. 3a and 3b to support further analysis. The rotor rotates clockwise, as shown in Fig. 3b. The MRF (multi-reference frames) method (Shahzad et al., 2022; Azlan et al., 2023) was adopted in this paper. The rotational zone of the model is shown in Fig. 3a, and the rest of the regions are stationary zones. By setting the angular velocity $\omega$ of the rotational zone to different values, the flow field characteristics at the corresponding $\omega$ could be obtained.

Air is considered an ideal gas with the physical properties shown in Table 2.

### 3.2 Numerical model setup

The maximum linear velocity of the rotor is 213 m/s=0.63*Ma*, making the model described in this paper a subsonic compressible flow model. Therefore, it is necessary to consider the effect of flow velocity on density change, that is, the compressibility of air. In consideration of the friction between the rotor and air, and between the air and the wall of the machine room, the energy equation and viscous heating options need to be checked.

In the momentum equation, for high-speed rotating flows, the PRESTO! scheme was selected for the pressure interpolation scheme (ANSYS, 2022a). Then the second-order upwind scheme was selected for the rest, and the semi-implicit method for pressure-linked equation (SIMPLE) algorithm was adopted as the pressure–velocity coupling scheme. Lastly, the shear stress transport (SST) turbulence model was selected

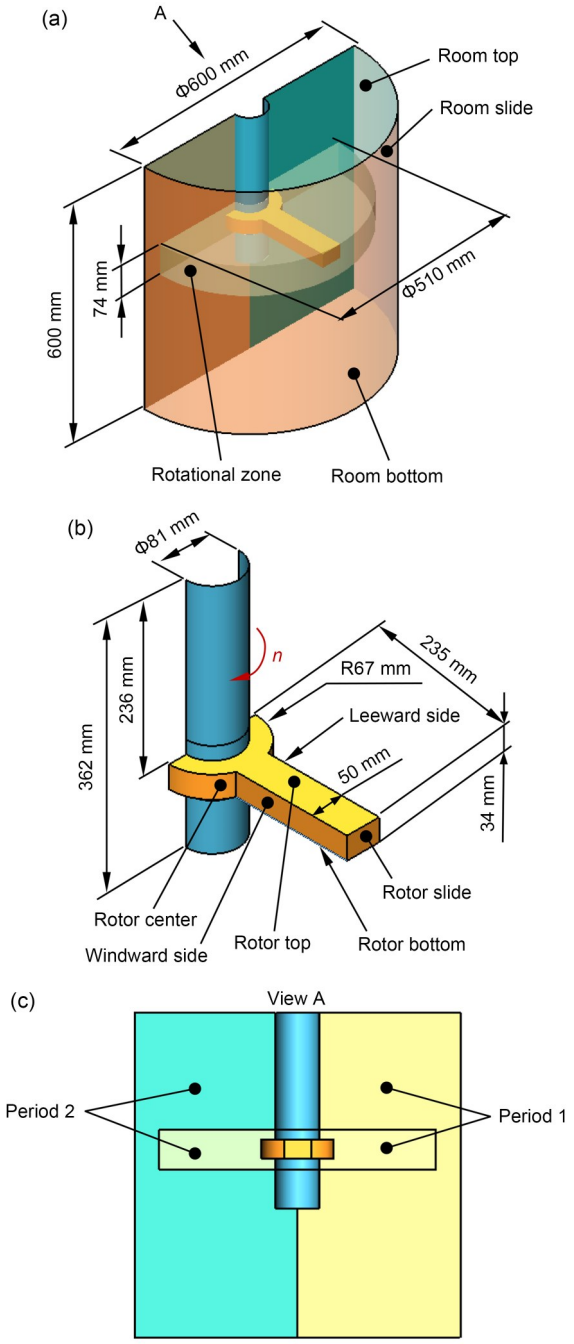


**Fig. 3 CFD calculation model: (a) naming of machine room walls; (b) naming of rotor walls; (c) a pair of periodic boundary interfaces**

**Table 2 Physical properties of air**

| Parameter | Value |
|---|---|
| Molecular weight (kg/kmol) | 28.966 |
| Viscosity (Pa·s) | $1.7894\times10^{-5}$ |
| Specific heat (J/(kg·K)) | 1006.3 |
| Thermal conductivity (W/(m·K)) | 0.0242 |

to solve the RANS equation because of its high reliability in rotating machinery with high speed (Menter, 1994; Guo et al., 2021; Wang et al., 2022). The automatic wall treatment was used to solve the flow field near the wall. It allows a consistent $y+$ insensitive mesh refinement from coarse meshes, which do not resolve the viscous sublayer, to fine meshes placing mesh points inside the viscous sublayer (Menter et al., 2003; ANSYS, 2022b).

The residual convergence was set to $1\times10^{-6}$ for the moment $T$, average velocity of the whole flow field $v_{ave}$, equations of energy, turbulent kinetic energy, and specific dissipation rate to achieve a balance between the computation accuracy and time.

### 3.3 Grid convergence index (GCI) method and model validation

Three models with different numbers of hexahedral structured grids ($N_1$=5621658, $N_2$=1491906, and $N_3$=509226) were analyzed. The grid of $N_1$ is shown in Fig. 4.

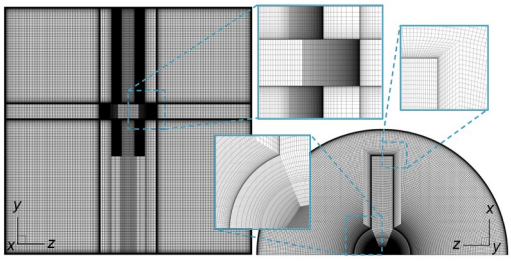

**Fig. 4 Grid of the scaled model device**

The grid convergence errors of the three different sets of grids were evaluated by a GCI method, as recommended by the American Society of Mechanical Engineers (ASME). Further details are shown in reference (Celik et al., 2008). Discretization error bars are shown in Fig. 5 (i.e., "$T_w$-CFD" and "$P_w$-CFD", where $P_w$ is calculated by $T_w\cdot\omega$), along with the $N_1$ grid solution. The maximum discretization uncertainty of GCI under the grid number $N_1$ was only 1.3049%. Thus, the simulation results under the grid number $N_1$ could be used for further analysis.

The results of the experiment from Table 1 are also presented in Fig. 5. The figure shows that the results of CFD simulation are in good agreement with the experimental results, indicating that the model presented in this study is reasonable and can accurately reflect the physical characteristics of the scaled model device.

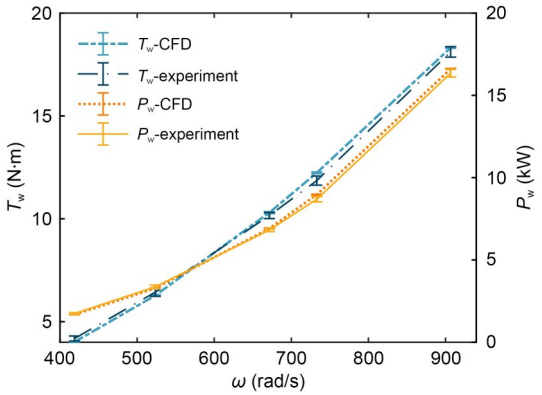


**Fig. 5 Comparison of results from CFD calculation and experiment**

## 4 Results and discussion

The existing calculation equation of the windage power, derived from the aerodynamic resistance equation, is as follows (Jia, 2013):

$$P_w=\sum P_{wi}=\sum T_{wi}\cdot\omega=\sum\int \mathrm{d}F_{wi}\cdot r_i\cdot\omega, \tag{7}$$

$$\mathrm{d}F_{wi}=\frac{1}{2}\rho_{\infty i}V_{\infty i}^2C_i\mathrm{d}S_i=\frac{1}{2}\rho_{\infty i}\alpha^2r_i^2\omega^2C_i\mathrm{d}S_i, \tag{8}$$

where $i$ denotes a rotating part (e.g., basket) or a rotating region (e.g., windward side of a rotating arm); $P_w$ denotes the total windage power of the device; $T_{wi}$ and $P_{wi}$ denote the windage moment and windage power on the $i$th part (region), respectively; $\mathrm{d}F_{wi}$ denotes the drag force over the area of $\mathrm{d}S_i$; $S_i$ denotes the windward wall area of $i$; $r_i$ denotes the radius from a point on a rotating part (region) $i$ to the center of rotation; $V_i$ denotes the linear velocity at a point on a rotating part (region) $i$; $\rho_{\infty i}$ and $V_{\infty i}$ are the free-stream density and velocity of a rotating part (region) $i$, respectively. $V_{\infty i}$ was set as $V_{\infty i}=\alpha V_i=\alpha r_i\omega$.

To thoroughly examine the distribution law of the windage power and derive the calculation equation, the results of the simulation in the last section are analyzed in this section. Firstly, the windage moment on the rotor is quantified to identify the key parts (regions) that affect the windage power. Then, the variation law of key parameters, that is, $\alpha$, $C_i$, and $\rho_{\infty i}$ in Eq. (8), in key regions is explored. Finally, the calculation equation of the windage power is derived according to the variation law.

### 4.1 Analysis of windage moment

It is necessary to quantify the proportion of the windage power in different regions to identify the key regions that affect the windage power. The windage power of the centrifuge can be calculated by multiplying the windage moment and the angular velocity on the rotating arm. When the rotating arm speed is determined, the angular velocity is also determined as a constant. This means that the distribution law of the windage moment can represent the distribution law of the windage power on the rotating arm. Therefore, the ratio of the calculated windage power in each region on the rotating arm is equivalent to that of the calculated windage moment. The force analysis of the air inside the closed room shows that the air rotates under the driving moment produced by the rotor (accordingly, the walls of the rotor are subjected to the resisting moment from the air), and at the same time, it is subjected to the action of the frictional resisting moment from the walls of the room. The air is in a state of dynamic equilibrium under the action of both forces.

#### 4.1.1 Moment component analysis

The moment on the walls can be divided into two categories: the moment caused by pressure and the frictional moment caused by shear stress. The moment caused by pressure can be calculated by multiplying the pressure by the area of the acting surface, and the moment caused by shear stress can be calculated using the following equations (ANSYS, 2022c):

$$T=\left\{\int[\boldsymbol{r}\times(\bar{\bar{\boldsymbol{\tau}}}\cdot\hat{\boldsymbol{n}})]\,\mathrm{d}S\right\}\cdot\hat{\boldsymbol{a}}, \tag{9}$$

$$\bar{\bar{\boldsymbol{\tau}}}\cdot\hat{\boldsymbol{n}}=\begin{bmatrix}\tau_{xx} & \tau_{xy} & \tau_{xz}\\ \tau_{yz} & \tau_{yy} & \tau_{yz}\\ \tau_{zx} & \tau_{zy} & \tau_{zz}\end{bmatrix}\cdot\begin{bmatrix}n_x\\ n_y\\ n_z\end{bmatrix}, \tag{10}$$

where $\boldsymbol{r}$ is the position vector; $\bar{\bar{\boldsymbol{\tau}}}$ is the total stress tensor; $\hat{\boldsymbol{n}}$ is a unit vector normal to the surface; $S$ is the surface comprising all rotating parts; $\hat{\boldsymbol{a}}$ is a unit vector parallel to the axis of rotation. Thus, the geometric and physical quantities on each wall element were extracted and the moments on each wall of the room and rotor were calculated (the moment on the rotor shaft was ignored since it accounted for only 0.03% of the total moment). The moments caused by pressure and shear stress were also calculated to distinguish the main factors of each wall moment. The calculated results are shown in Table 3. The ratio of the moment at each wall is divided into two groups according to the aforementioned moment equilibrium: the dimensionless moment on rotor walls or on room walls. In dimensionless quantity calculation, the maximum value of the physical quantity across the entire field is taken as the reference value, and other values are divided by this reference value.

Table 3 shows that the absolute value of the total resistance moment of each wall of the room is almost the same as that of the rotor, with a difference of only 0.7%–0.8%. The difference is regarded as the convergence error, so it can be verified that the air in the room is in a balanced state under the action of the rotor driving moment and the resistance moment of the walls. In terms of the proportion of moment, the ratio of the moment on each wall of the room or rotor is essentially consistent for different $\omega$. The windward and leeward

**Table 3 Proportion of moment in each region**

| Item | Region | Proportion of moment | | | | |
|---|---|---|---|---|---|---|
| | | $\omega$=418.68 rad/s | $\omega$=523.56 rad/s | $\omega$=671.60 rad/s | $\omega$=733.04 rad/s | $\omega$=906.75 rad/s |
| Room | Bottom | −9.8% | −9.8% | −9.8% | −9.8% | −9.7% |
| | Side | −80.6% | −80.6% | −80.6% | −80.6% | −80.7% |
| | Top | −10.4% | −10.4% | −10.4% | −10.3% | −10.3% |
| | Total | −100.8% | −100.8% | −100.8% | −100.7% | −100.7% |
| Rotor | Center | 0.0% | 0.0% | 0.0% | 0.0% | 0.0% |
| | Bottom | 0.5% | 0.5% | 0.5% | 0.5% | 0.5% |
| | Top | 0.5% | 0.5% | 0.5% | 0.5% | 0.5% |
| | Side | 0.2% | 0.2% | 0.2% | 0.2% | 0.1% |
| | Windward | 69.4% | 69.8% | 70.2% | 69.9% | 70.0% |
| | Leeward | 29.4% | 29.0% | 28.6% | 28.9% | 28.9% |
| | Total | 100.0% | 100.0% | 100.0% | 100.0% | 100.0% |

walls of the rotor are subjected to about 99% of the total moment, with the windward wall accounting for about 69% and the leeward wall for about 30%. The moment on the side wall of the room accounts for 80% of the total moment, and the top and bottom wall moments each account for about 10%.

To clarify the contribution of pressure and shear stress to the moment, the results at $\omega$=906.75 rad/s were used to quantify the proportion of moment due to pressure and shear stress on each wall (Huang et al., 2023). The results are shown in Table 4, where "total" indicates the total proportion of moments caused by pressure and shear stress on the rotor walls. The moment on the rotor results mainly from the pressure on the walls, while the moment caused by the shear stress accounts for only 0.7% of the total moment, which is caused mainly by the friction between the top, bottom, and center walls and the air. Therefore, the aerodynamic characteristics of the rotor are the crucial factor affecting the windage moment.

**Table 4 Proportion of moment component at $\omega$=906.75 rad/s**

| Item | Region | Proportion of moment | |
|---|---|---|---|
| | | Pressure | Shear stress |
| Room | Bottom | 0.0% | −9.7% |
| | Side | 0.0% | −80.7% |
| | Top | 0.0% | −10.3% |
| Rotor | Center | 0.0% | 0.0% |
| | Bottom | 0.0% | 0.5% |
| | Top | 0.0% | 0.5% |
| | Side | 0.2% | −0.1% |
| | Windward | 69.9% | 0.1% |
| | Leeward | 29.1% | −0.2% |
| | Total | 99.3% | 0.7% |

The resistance moment on the walls of the room is the frictional moment caused by the shear stress, which comes from the viscous effect of the air. The frictional moment is related to the wall area. According to Fig. 3, the proportion of area on the side, top, and bottom walls of the machine room is 66.6%, 16.7%, and 16.7%, respectively. This means that the side area is the largest. Therefore, in Table 3, the moment of force of the side wall is the greatest. However, the proportion of wall moment and area in the machine room is not exactly the same. This is because the rotor is located in the center of the room, and as the air is accelerated and flows towards the top and bottom walls, the velocity decreases. This results in the air flow velocity being higher on the room side wall than on the top and bottom walls, and causes the shear stress on the side wall to be the highest. As shown by the dimensionless shear stress contour shown in Fig. 6, the shear stress around the rotor is significantly higher than on the top and bottom walls of the room, indicating that the aerodynamic characteristics of the rotor are the key reason for the high proportion of stress on the side wall.

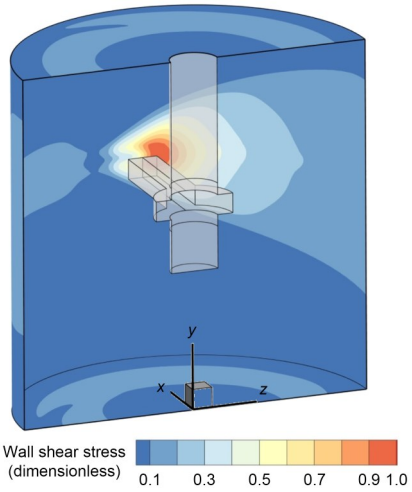


**Fig. 6 Shear stress contours of machine room walls**

4.1.2 Moment distribution law on the rotor windward and leeward walls

According to the analysis in the last section, most of the moment consumption on the rotor occurs on the windward and leeward walls, so the moment on these walls is quantified in this section. Since the proportion of moment in each region under different angular velocities is basically very similar, only the results at the highest angular velocity are taken for the analysis of the results. The results are dimensionless to make them more universal.

Fig. 7 shows the distribution law of pressure and velocity around the rotor. Figs. 7a and 7b show the dimensionless pressure contours on the windward and leeward walls of the rotor, respectively. The rightmost side of each contour corresponds to the end face of the rotor. Fig. 7a shows that the pressure on the windward wall is positive, because the air is blocked by the windward wall. The flow velocity slows down, then the pressure increases, and a high-pressure area appears in the end region of the rotor. From Fig. 7b, the leeward pressure is mainly negative. To illustrate the cause

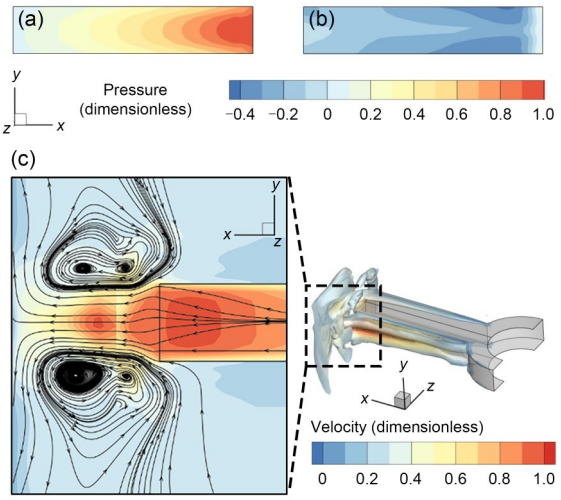


**Fig. 7 Distribution law of pressure and velocity around the rotor: (a) windward wall pressure contour; (b) leeward wall pressure contour; (c) vortex contour**

of this phenomenon, Fig. 7c shows the vortex contour isosurface near the leeward wall (shown on the right), which is calculated by the $Q$-criterion where $Q$=5×10$^6$. The streamline graph of the particles near the end of the leeward wall is shown on the left side of Fig. 7c. Many vortexes are generated on the upper and lower sides of the end region, forming a vortex zone, which dramatically increases the flow velocity of the air in this region and results in a decrease in pressure and a negative pressure zone.

From the analysis above, the end area of the rotor is a high-pressure area that is equipped with a test basket or a counterbalance basket, making it a crucial location for the test, whether it is on the leeward or windward wall. So the following quantification technique is proposed to quantify the amount of moment in this region:

$$p_{\mathrm{T}}(r_{\mathrm{rel},0}) = \frac{1}{T_{\mathrm{tol}}} \int_0^{r_{\mathrm{rel},0}} T(r_{\mathrm{rel}})\,\mathrm{d}r_{\mathrm{rel}}, \tag{11}$$

where $r_{\mathrm{rel}}$ denotes the relative radius of the rotor; $T(r_{\mathrm{rel}})$ denotes the moment at the relative radius $r_{\mathrm{rel}}$; $T_{\mathrm{tol}}$ denotes the sum of the moment in the length direction of the rotor; $p_{\mathrm{T}}(r_{\mathrm{rel},0})$ denotes the proportion of the total moment on the interval [0, $r_{\mathrm{rel},0}$]; $r_{\mathrm{rel},0}$ represents the current relative radius, which varies from 0 to 1.

The moment distribution along with $r_{\mathrm{rel}}$ at different $\omega$ was analyzed by the quantification method. The values on elements with the same radius area were accumulated and the results are shown in Fig. 8, where $\omega_1$–$\omega_5$ represent the speeds of 418.68–906.75 rad/s (Table 3), the subscript "wind" indicates the windward wall, the subscript "lee" indicates the leeward wall, and the subscript "tol" indicates the cumulative result of the windward and leeward walls. The curves at different speeds almost completely coincide, indicating that the distribution of moment is independent of the speed. As $\omega$ increases, $p_{\mathrm{T}}$ shows an exponential increase, which means that the moment in the small area at the end of the rotor will be subject to most of the total moment. Taking a CHIEF machine as an example, the interval of the average relative radius of the basket is [0.69, 1], and the moment in this interval accounts for 72% of the total moment, indicating the basket is the key part that affects the windage power of the geotechnical centrifuge. However, the moment on the rotating arm also accounts for 28%, which should not be underestimated for a large geotechnical centrifuge. Therefore, the influence of the rotating arm cannot be ignored in the selection of key parts.

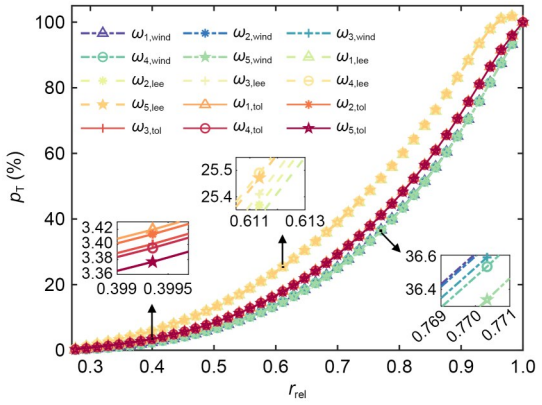


**Fig. 8 Comparison of the distribution law of the moment along with $r_{\mathrm{rel}}$ on the windward wall, leeward wall, and rotor at different $\omega$**

## 4.2 Analysis of key parameters

According to the above analysis, the windward and leeward walls of the rotor are the key regions affecting the windage power, so the subscript $i$ in Eq. (8) could be regarded as the windward wall or leeward wall. The variation rules of the key parameters $\alpha$ and $C_i$ on the windward and leeward walls were analyzed.

To calculate $\alpha$ and $C_i$, the plane where the air linear velocity $V_\infty$ and air density $\rho_\infty$ are located should first be determined. This plane should be located far ahead of the direction of motion, so it can be defined on the

radial plane farthest from the rotor for the rotating flow field, i.e., the areas in "Period 1" and "Period 2" in Fig. 3 corresponding to the windward and leeward walls. The plane is called the $S_\infty$ plane. Thus, $\rho_\infty$ and $V_\infty$ at any $r_i$ in the $S_\infty$ plane can be easily obtained. The velocity coefficient $\alpha$ can be solved by $V_\infty=\alpha r_i\omega$. The drag force $F_{wi}$ at any $r_i$ of the windward and leeward walls of the rotor can be obtained by multiplying the pressure and the area of the elements. Then, the windage coefficient $C_i$ at any $r_i$ can be determined by Eq. (8). Due to the periodic symmetry of the flow field in the room, the physical quantities $V_\infty$, $\rho_\infty$, and $\alpha$ are the same in the two $S_\infty$ planes corresponding to the windward and leeward walls. But the resistance moment of the windward and leeward walls is different, so the $C_i$ is also different. The variation rules of $\rho_\infty$, $\alpha$, and $C_i$ are shown in Fig. 9.

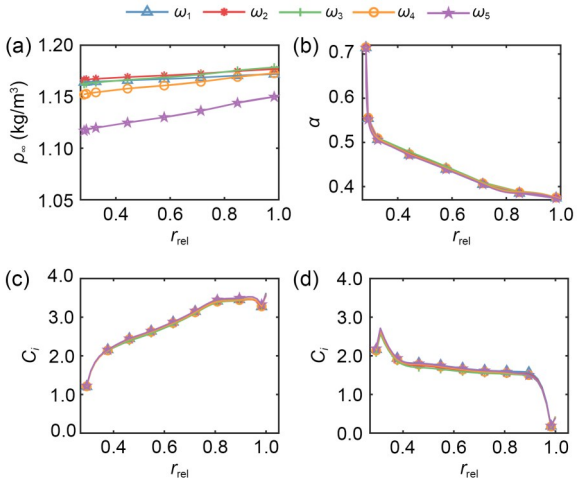


**Fig. 9 Variation rules of $\rho_\infty$ (a), $\alpha$ (b), and $C_i$ (c) on the windward wall and $C_i$ (d) on the leeward wall along with $r_{rel}$ at different $\omega$**

Fig. 9a shows the variation rules of $\rho_\infty$ along with $r_{rel}$ at different $\omega$. $\rho_\infty$ increases with the increase of $r_{rel}$ at different $\omega$, but the fluctuation range is small. The average density $\bar{\rho}_\infty$ is $\bar{\rho}_\infty=(1.1450\pm0.0270)$ kg/m$^3$ (the deviation indicates the fluctuation range of $\rho_\infty$ at different $\omega$ and $r_{rel}$). As the fluctuation range is so small, $\rho_\infty$ can be considered a constant value in engineering calculations.

Fig. 9b shows the variation rules of the velocity coefficient $\alpha$ along with $r_{rel}$ at different $\omega$. $\alpha$ is slightly influenced by $\omega$, with a maximum deviation of 1.6%. The curve consists of three stages determined by the relative radius. The first stage is in interval [0.28, 0.35], which is located near the wall "rotor center" where the linear velocity of the rotor is low and $\alpha$ is large, indicating that the synchronization between air and rotor motion is good. According to Table 4, the moment on the "rotor center" wall is caused mainly by the shear stress, i.e., the viscosity plays a leading role, and the air is "stuck" in the near wall area. Once far away from the near wall area, $\alpha$ decreases sharply. The second stage is in interval [0.35, 0.8]. The air nearby is driven by the rotor and flows toward the $S_\infty$ plane. Since the influence of the rotor is continuously weakened in the flow direction and the kinetic energy of the air dissipates gradually under the viscous effect between the air near and far from the "rotor center" wall, finally the velocity coefficient $\alpha$ shows a linear decrease. The third stage is in interval [0.8, 1], which is located in the circumferential range of the rotor end. Fig. 7c shows that a vortex appears here and the flow state is rather complicated. The variation of $\alpha$ tends to be gentle, with a maximum in this interval of only 3.7%.

Figs. 9c and 9d show the variation rules of $C_i$ on the windward wall and leeward wall, respectively, along with $r_{rel}$ at different $\omega$. When $r_{rel}$ is less than about 0.35, $C_i$ of the leeward wall is higher than that of the windward wall. But when $r_{rel}$ is greater than 0.35, the changing trend of $C_i$ is the opposite. The average values of $C_i$ for the windward wall and leeward wall at each $\omega$ along with $r_{rel}$ are 2.8208 and 1.6041. The average rotor total windage coefficient is 4.4249, calculated as the sum of the values for the windward and leeward walls. The maximum deviation at different $\omega$ for the total windage coefficient is 4.24%, indicating that $C_i$ was little affected by $\omega$.

### 4.3 Windage power calculation equation

According to Section 4.1, the windage moment on the windward and leeward walls of the rotor plays a dominant role, so only the windward and leeward walls are considered in the calculation (the error caused by ignoring other walls is about 1%). Besides, $r_{rel}$ and $\omega$ have little effect on $\rho_\infty$, so $\rho_\infty$ can be considered a constant, and thus $\rho_\infty=\bar{\rho}_\infty$. From Section 4.2, $\alpha$ and $C_i$ are related to the relative radius $r_{rel}$ of the rotor and are almost independent of the angular velocity $\omega$. Therefore, $\alpha$ and $C_i$ can be assumed to be a function of only $r_{rel}$ of the rotor. Set the rotor radius as $r_a$, then $r_{rel}=r_i/r_a$ and $\mathrm{d}r_{rel}=r_a^{-1}\mathrm{d}r_i$. In addition, the rotor cross section is rectangular in the model of this study, so $\mathrm{d}S_i=b\mathrm{d}r_i$ in

Eq. (8), where $b$ is the height of the rotor. The windage power is calculated by considering the rotor as a whole and no longer distinguishes between the windward and leeward walls, so Eq. (7) can be rewritten as:

$$P_w=\frac{1}{2}\bar{\rho}_\infty b r_a^4\omega^3\int C_i(r_{rel})[\alpha(r_{rel})]^2 r_{rel}^3 \mathrm{d}r_{rel}. \quad (12)$$

Make $\Phi=\int\varphi \mathrm{d}r_{rel}$, where $\varphi=C_i(r_{rel})[\alpha(r_{rel})]^2 r_{rel}^3$. Based on the calculation results in Section 4.2, $\Phi$=(0.3732±0.0008) and the deviation of $\Phi$ for different $\omega$ is only 0.43%. Therefore, the previous assumption that taking $\rho_\infty$ as a constant and ignoring the effect of $\omega$ on $\alpha$ and $C_i$ is reasonable. Moreover, it can be considered that $\Phi$ is related only to $r_{rel}$. If the geometric size of the machine is determined, $\Phi$ is a constant value, so it can be regarded as an inherent parameter of the machine. The maximum radius of the rotor is chosen as the denominator for normalization for the calculation of $\Phi$, which can be referred to as the characteristic length. Other parameters, such as the room's radius $R$, can also be used to determine the characteristic length, and then $\Phi_R=\Phi_{r_a}\cdot(r_a/R)^4$.

### 4.4 Idle power effect

According to Section 4.3, $\Phi$ is independent of $\omega$. Then Eq. (12) can be written in the following form:

$$P_w=K_w\omega^3. \quad (13)$$

In contrast, the power of $\omega$ is considered not equal to 3 in the literature (Wang et al., 2014; Guo et al., 2020a, 2020b, 2021), i.e., $q\neq3$ in Eq. (14). But it is based on fitting the total power curve, which may not exclude the influence of the idle power. To clarify the influence of the idle power on the total power function form, the relationship between the idle power and the total power of the test device was investigated.

$$P=K\omega^q. \quad (14)$$

Table 5 shows the proportion of the idle power to the total power of the device at different $\omega$. The proportion of the idle power decreases gradually with the increase of $\omega$. At low $\omega$, the idle power accounts for 32%, which will introduce a large error if the total power is considered as the windage power. However, even at the highest angular speed, the idle power still remains at 12%, which will have a non-negligible influence on the function form of the total power. Therefore, the idle power should not be ignored in exploring the variation rules of the windage power, and its influence should also be excluded from the total power.

**Table 5 Proportion of idle power at different $\omega$**

| $\omega$ (rad/s) | Proportion of idle power, $P_h/P_t$ |
|---|---|
| 418.68 | 32% |
| 523.56 | 25% |
| 671.60 | 19% |
| 733.04 | 17% |
| 906.75 | 12% |

Fig. 10 shows the idle power and total power curves of the test device (corresponding to $P_h$ and $P_t$, respectively). $P_h$ can be well fitted by the power function Eq. (15):

$$P_h=K_h\omega^{q_h}. \quad (15)$$

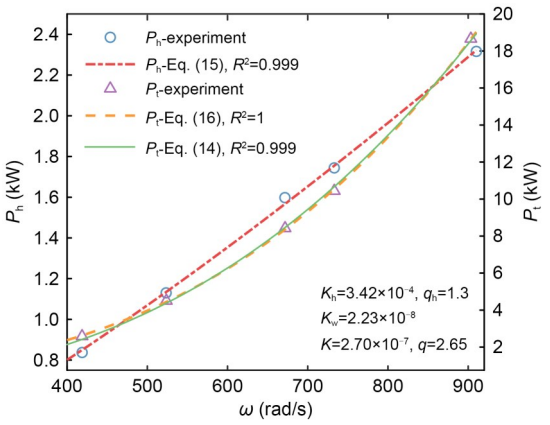


**Fig. 10 The idle power $P_h$ and the total power curve**

Then, the total power can be expressed as:

$$P_t=P_w+P_h=K_w\omega^3+K_h\omega^{q_h}. \quad (16)$$

The total power was fitted using Eq. (16) and Eq. (14) separately, and the fitting results are shown in Fig. 10, where $R^2$ is the correlation coefficient. The values of the parameters in the equations are also shown in the lower right corner of the figure.

Fig. 10 shows that both Eq. (16) and Eq. (14) can fit the total power curve well, but the $R^2$ of Eq. (16) is slightly larger than that of Eq. (14). This means that the function form of Eq. (16) seems to be more suitable

for characterizing the total power, which verifies to some extent that $q \neq 3$ in Eq. (14) is caused by not eliminating the idle power.

The total power data in the literature (Wang et al., 2014; Guo et al., 2020a, 2020b, 2021) were fitted (original data are from Yin et al. (2010a, 2010b) and Guo et al. (2020a)) to further explain the universality of Eq. (16). To plot the power curves of the different devices in one figure, the data are normalized, i.e., the maximum values of $\omega$ and $P_t$ are taken as reference values for the horizontal and vertical coordinates, respectively, and other values are divided by these reference values to obtain dimensionless relative values. The normalization does not affect the power of $\omega$. The fitting results are shown in Fig. 11. The $R^2$ of all three curves is 1, verifying again the accuracy of Eq. (16).

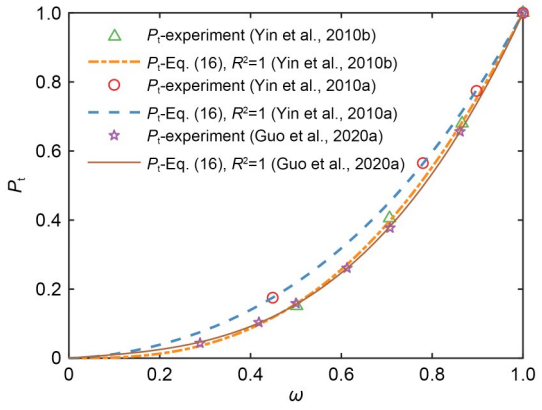


**Fig. 11 Total power data from the literature (Yin et al., 2010a, 2010b; Guo et al., 2020a) fitted via Eq. (16)**

Table 6 shows a comparison of the size of the three geotechnical centrifuges in Fig. 11 and the scaled model in this paper. Although there are significant differences in the size of these four devices, Eq. (16) obtained in this study can well fit the power characteristics of these devices, demonstrating the adaptability of Eq. (16) and the correctness of the windage power law analysis.

**Table 6 Geotechnical centrifuge size**

| Centrifuge | Room radius (m) | Room height (m) | Rotor radius (m) | $R^2$ |
|---|---|---|---|---|
| Yin et al. (2010a) | 2.6 | 2.8 | 2.2 | 1 |
| Yin et al. (2010b) | 4.0 | 3.8 | 3.0 | 1 |
| Guo et al. (2020a) | 5.4 | 4.3 | 5.0 | 1 |
| This paper | 0.60 | 0.60 | 0.47 | – |

Another problem caused by replacing the windage power with total power is that it is difficult to obtain a universal equation for calculating the windage power. Since the idle power is related to the aging of the equipment and the lubrication state of the transmission system, even if two devices with identical geometric dimensions are running under the same working condition, the total power may vary greatly due to the different operating states of the equipment. Thus, the idle power is equivalent to a random quantity, which will cause the total power of the two devices to show different random characteristics. Once the randomness is introduced, the obtained windage power calculation equation will be more specific rather than universal.

In addition, when the power of $\omega$ in the expression of windage power is determined to be a constant 3, only a constant speed test is needed to explore the influence factor of the windage power for a fixed device, which will considerably reduce the test workload.

## 5 Conclusions

In this study, an experimental method was conducted to determine the windage power and idle power of a CHIEF-scaled model device, and then the rationality of the CFD model was validated. The movement law of the flow field in the device was investigated using CFD simulation. The key areas affecting the windage power were identified, and the errors caused to the key parameters by neglecting the speed were evaluated. Finally, a new simplified windage power calculation equation was proposed based on eliminating the influence of idle power. Therefore, the conclusions of this paper can be drawn as follows:

1. It is necessary to evaluate the effect on the windage power of error transfer introduced by indirect measurement methods.

2. The windage power on the basket and the rotating arm accounts for 72% and 28% of the total windage power, respectively. This shows that the basket is the key part, but the role of the rotating arm cannot be ignored in the selection of key parts.

3. The velocity coefficient and windage coefficient are related to the geometric size of the device and are almost independent of the angular velocity. So, the influence of angular velocity can be disregarded while exploring the impact of the equipment's geometrical

dimensions on the windage power, which will greatly simplify the test and design thereafter.

4. The windage power is proportional to the cube of the angular velocity after eliminating the effect of idle power.

## Acknowledgments

This work is supported by the National Major Science and Technology Infrastructure Project of China (No. 2017-000052-73-01-002083) and the Information Technology Center, Zhejiang University, China.

## Author contributions

Chuanxiang ZHENG and Yuchen DAI designed the research. Jiao LIN and Yuchen DAI processed the corresponding data. Yuchen DAI and Jiao LIN wrote the first draft of the manuscript. Jinjie LU, Jianqun JIANG, Zhenyu WANG, and Jiaming YAN helped to organize the manuscript. Chuanxiang ZHENG, Yuchen DAI, and Jiao LIN revised and edited the final version.

## Conflict of interest

Chuanxiang ZHENG, Yuchen DAI, Jiao LIN, Jianqun JIANG, Jinjie LU, Zhenyu WANG, and Jiaming YAN declare that they have no conflict of interest.

## References

ANSYS, 2022a. 2.8.1.3. Automatic near-wall treatment for omega-based models. *In*: ANSYS CFX-Solver Theory Guide. ANSYS Inc., USA.

ANSYS, 2022b. 32.3.3. Choosing the pressure interpolation scheme. *In*: ANSYS Fluent 2022 R1 Users Guide. ANSYS Inc., USA.

ANSYS, 2022c. 2.3.2.7. Swirl conservation. *In*: ANSYS Fluent 2022 R1 Theory Guide. ANSYS Inc., USA.

Azlan F, Tan MK, Tan BT, et al., 2023. Passive flow-field control using dimples for performance enhancement of horizontal axis wind turbine. *Energy*, 271:127090. https://doi.org/10.1016/j.energy.2023.127090

Balakrishnan S, Viswanadham BVS, 2019. Centrifuge model studies on the performance of soil walls reinforced with sand-cushioned geogrid layers. *Geotextiles and Geomembranes*, 47(6):803-814. https://doi.org/10.1016/j.geotexmem.2019.103496

Celik IB, Ghia U, Roache PJ, et al., 2008. Procedure for estimation and reporting of uncertainty due to discretization in CFD applications. *Journal of Fluids Engineering*, 130(7): 078001. https://doi.org/10.1115/1.2960953

Chanda D, Saha R, Haldar S, et al., 2023. State-of-the-art review on responses of combined piled raft foundation subjected to seismic loads using static and dynamic approaches. *Soil Dynamics and Earthquake Engineering*, 169:107869. https://doi.org/10.1016/j.soildyn.2023.107869

Chen SS, Gu XW, Ren GF, et al., 2020. Upgradation of NHRI-400 *g*·t geotechnical centrifuge. *Chinese Journal of Geotechnical Engineering*, 42(S2):7-12 (in Chinese). https://doi.org/10.11779/CJGE2020S2002

Costa CML, Zornberg JG, Bueno BDS, et al., 2016. Centrifuge evaluation of the time-dependent behavior of geotextile-reinforced soil walls. *Geotextiles and Geomembranes*, 44(2): 188-200. https://doi.org/10.1016/j.geotexmem.2015.09.001

Dai Y, Zhang YY, Zhu X, 2023. Generalized analytical model for evaluating the gear power losses transition changing from windage to churning behavior. *Tribology International*, 185:108572. https://doi.org/10.1016/j.triboint.2023.108572

Deng LJ, Kutter BL, Kunnath SK, 2012. Centrifuge modeling of bridge systems designed for rocking foundations. *Journal of Geotechnical and Geoenvironmental Engineering*, 138(3): 335-344. https://doi.org/10.1061/(ASCE)GT.1943-5606.0000605

Dong DJ, 2013. Error Analysis and Data Processing. Tsinghua University Press, Beijing, China (in Chinese).

Du YL, Zhu SZ, Liu LY, et al., 1992. Development of LXJ-4-450 centrifuge for geotechnical engineering. *Journal of Hydraulic Engineering*, 23(2):19-28 (in Chinese). https://doi.org/10.13243/j.cnki.slxb.1992.02.003

Gao ZW, Lu DC, Hou Y, et al., 2023. Constitutive modelling of fabric effect on sand liquefaction. *Journal of Rock Mechanics and Geotechnical Engineering*, 15(4):926-936. https://doi.org/10.1016/j.jrmge.2022.06.002

Garnier J, Gaudin C, Springman SM, et al., 2007. Catalogue of scaling laws and similitude questions in geotechnical centrifuge modelling. *International Journal of Physical Modelling in Geotechnics*, 7(3):1-23. https://doi.org/10.1680/ijpmg.2007.070301

Garzón LX, Caicedo B, Sánchez-Silva M, et al., 2015. Physical modelling of soil uncertainty. *International Journal of Physical Modelling in Geotechnics*, 15(1):19-34. https://doi.org/10.1680/ijpmg.14.00012

Guo YN, Yang Y, Jiang JQ, et al., 2020a. Analysis of influences of helium working medium replacement and operating pressure on wind resistance power of geotechnical centrifuge. *Earthquake Engineering and Engineering Dynamics*, 40(6):197-206 (in Chinese). https://doi.org/10.13197/j.eeev.2020.06.197.guoyn.020

Guo YN, Yang Y, Wang YL, et al., 2020b. CFD simulation method based on ZJU400 geotechnical centrifuge. *Equipment Environmental Engineering*, 17(11):85-89 (in Chinese). https://doi.org/10.7643/issn.1672-9242.2020.11.013

Guo YN, Yang Y, Yu JX, et al., 2021. A computational fluid dynamic-based method for analyzing the nonlinear relationship between windage loss and pressure in a geotechnical centrifuge. *SN Applied Sciences*, 3(10):791. https://doi.org/10.1007/s42452-021-04775-2

Hao Y, Yin YH, Wan Q, et al., 2018. Comparative study on estimation methods of wind resistance of geotechnical centrifuges. *Equipment Environmental Engineering*, 15(3):61-66 (in Chinese). https://doi.org/10.7643/issn.1672-9242.2018.03.013

Huang B, Zhang H, Ding YQ, 2023. CFD modelling and numerical simulation of the windage characteristics of a high-speed gearbox based on negative pressure regulation. *Processes*, 11(3):804. https://doi.org/10.3390/pr11030804

Iglesia GR, Einstein HH, Whitman RV, 2014. Investigation of soil arching with centrifuge tests. *Journal of Geotechnical and Geoenvironmental Engineering*, 140(2):04013005. https://doi.org/10.1061/(ASCE)GT.1943-5606.0000998

Jia PZ, 2013. Steady-State Acceleration Simulation Test Equipment—Centrifuge Conspectus and Design. National Defense Industry Press, Beijing, China (in Chinese).

Kutter BL, Li XS, Sluis W, et al., 1991. Performance and instrumentation of the large centrifuge at Davis. *Centrifuge*, 91: 19-26.

Lee FH, Schofield AN, 1988. Centrifuge modelling of sand embankments and islands in earthquakes. *Géotechnique*, 38(1):45-58. https://doi.org/10.1680/geot.1988.38.1.45

Lee FH, Lee CH, Dasari GR, 2006. Centrifuge modelling of wet deep mixing processes in soft clays. *Géotechnique*, 56(10):677-691. https://doi.org/10.1680/geot.2006.56.10.677

Leung CF, Lee FH, Yet NS, 2001. Centrifuge model study on pile subject to lapses during installation in sand. *International Journal of Physical Modelling in Geotechnics*, 1(1):47-57. https://doi.org/10.1680/ijpmg.2001.010105

Liang T, Bengough AG, Knappett JA, et al., 2017. Scaling of the reinforcement of soil slopes by living plants in a geotechnical centrifuge. *Ecological Engineering*, 109:207-227. https://doi.org/10.1016/j.ecoleng.2017.06.067

Lin WA, Zheng CX, Jiang JQ, et al., 2020. Temperature control test of scaled model of high capacity hypergravity centrifuge. *Journal of Zhejiang University (Engineering Science)*, 54(8):1587-1592 (in Chinese). https://doi.org/10.3785/j.issn.1008-973X.2020.08.018

Menter F, Carregal Ferreira J, Esch T, et al., 2003. The SST turbulence model with improved wall treatment for heat transfer predictions in gas turbines. Proceedings of the International Gas Turbine Congress, p.1-7.

Menter FR, 1994. Two-equation eddy-viscosity turbulence models for engineering applications. *AIAA Journal*, 32(8): 1598-1605. https://doi.org/10.2514/3.12149

Najser J, Pooley E, Springman SM, 2009. Modelling of double porosity clays in a mini-centrifuge. *International Journal of Physical Modelling in Geotechnics*, 9(1):15-22. https://doi.org/10.1680/ijpmg.2009.090102

Ng CWW, Zhang C, Farivar A, et al., 2020. Scaling effects on the centrifuge modelling of energy piles in saturated sand. *Géotechnique Letters*, 10(1):57-62. https://doi.org/10.1680/jgele.19.00051

Shahzad A, Pashak P, Lazoglu I, 2022. A novel unibody axial flow pump for the lubrication of inverter type hermetic reciprocating compressors. *International Journal of Refrigeration*, 140:1-8. https://doi.org/10.1016/j.ijrefrig.2022.04.019

Shao WB, Ren XD, Hu B, 2022. Numerical simulation on temperature rise of high-speed geotechnical centrifuge. *Equipment Environmental Engineering*, 19(12):95-103 (in Chinese). https://doi.org/10.7643/issn.1672-9242.2022.12.014

Song DR, Zhou GD, Choi CE, et al., 2019. Scaling principles of debris flow modeling using geotechnical centrifuge. *Chinese Journal of Geotechnical Engineering*, 41(12): 2262-2271 (in Chinese). https://doi.org/10.11779/CJGE201912011

Sun SZ, 1991. Review of design for geotechnical centrifuge (II). *Journal of Nanjing Hydraulic Research Institute*, (2): 219-226 (in Chinese). https://doi.org/10.16198/j.cnki.1009-640x.1991.02.011

Take WA, Bolton MD, 2011. Seasonal ratcheting and softening in clay slopes, leading to first-time failure. *Géotechnique*, 61(9):757-769. https://doi.org/10.1680/geot.9.P.125

Wang MC, Li YJ, Yuan JP, et al., 2022. Effects of different vortex designs on optimization results of mixed-flow pump. *Engineering Applications of Computational Fluid Mechanics*, 16(1):36-57. https://doi.org/10.1080/19942060.2021.2006091

Wang YZ, Chen ZS, Sun R, 2014. Simplified calculation technique of steady-state wind resistance power for geotechnical centrifuge and optimization cooling design. *Earthquake Engineering and Engineering Dynamics*, 34(S1): 909-914 (in Chinese). https://doi.org/10.13197/j.eeev.2014.S0.909.wangyz.143

Watson PG, Randolph MF, 1998. Skirted foundations in calcareous soil. *Proceedings of the Institution of Civil Engineers-Geotechnical Engineering*, 131(3):171-179. https://doi.org/10.1680/igeng.1998.30473

White DJ, Take WA, Bolton MD, 2003. Soil deformation measurement using particle image velocimetry (PIV) and photogrammetry. *Géotechnique*, 53(7):619-631. https://doi.org/10.1680/geot.2003.53.7.619

Woodward PK, Brennan A, Laghrouche O, et al., 2022. Geotechnical centrifuge and full-scale laboratory testing for performance evaluation of conventional and high-speed railway track structures. *In*: Tutumluer E, Nazarian S, Al-Qadi I, et al. (Eds.), Advances in Transportation Geotechnics IV. Springer, Cham, Switzerland, p.957-968. https://doi.org/10.1007/978-3-030-77234-5_78

Yan JM, Lin ZY, Sun WJ, et al., 2022. Effects of cavity vacuum degree on wind resistance and thermal environment of high-speed geotechnical centrifuge. *Equipment Environmental Engineering*, 19(10):120-125 (in Chinese). https://doi.org/10.7643/issn.1672-9242.2022.10.016

Yin YH, Yu SR, Feng XJ, et al., 2010a. Aerodynamic power of geotechnical centrifuges with closed chamber. *Journal of Mianyang Normal University*, 29(2):1-5 (in Chinese). https://doi.org/10.3969/j.issn.1672-612X.2010.02.001

Yin YH, Yu SR, Feng XJ, et al., 2010b. Aerodynamic power of geotechnical centrifuges with holed chamber. *Journal of Mianyang Normal University*, 29(5):1-5 (in Chinese). https://doi.org/10.3969/j.issn.1672-612X.2010.05.001

Yin YH, Hao Y, Li QS, et al., 2018. An analysis on air pressure and natural air exhausting in the work chamber of a steadily

running rotary arm type centrifuge. *Journal of Mianyang Normal University*, 37(11):1-6 (in Chinese). https://doi.org/10.16276/j.cnki.cn51-1670/g.2018.11.001

Yin YH, Li QS, Hao Y, et al., 2020. Research on transient temperature in the work room of a rotary arm type centrifuge. *Applied Mathematics and Mechanics*, 41(1): 81-97 (in Chinese). https://doi.org/10.21656/1000-0887.400047

Zeng X, Lim SL, 2002. The influence of variation of centrifugal acceleration and model container size on accuracy of centrifuge test. *Geotechnical Testing Journal*, 25(1):24-43. https://doi.org/10.1520/GTJ11077J

Zhang YT, Li JD, An XY, et al., 2019. Construction and Application of TK-C500 Geotechnical Centrifuge Laboratory. People's Communications Press, Beijing, China (in Chinese).

Zhang ZH, Li Y, Xu CS, et al., 2021. Study on seismic failure mechanism of shallow buried underground frame structures based on dynamic centrifuge tests. *Soil Dynamics and Earthquake Engineering*, 150:106938. https://doi.org/10.1016/j.soildyn.2021.106938

Zheng CX, Chen JY, Jiang JQ, et al., 2020. Experiment of heat generation mechanism of geotechnical centrifuge under low vacuum degrees. *Equipment Environmental Engineering*, 17(3):84-88 (in Chinese). https://doi.org/10.7643/issn.1672-9242.2020.03.014

Zhu X, Dai Y, 2023. Development of an analytical model to predict the churning power losses of an orthogonal face gear. *Engineering Science and Technology, an International Journal*, 41:101383. https://doi.org/10.1016/j.jestch.2023.101383